

# Tensor-Based Cortical Surface Morphometry via Weighted Spherical Harmonic Representation

Moo K. Chung\*, Kim M. Dalton, and Richard J. Davidson

**Abstract**—We present a new tensor-based morphometric framework that quantifies cortical shape variations using a local area element. The local area element is computed from the Riemannian metric tensors, which are obtained from the smooth functional parametrization of a cortical mesh. For the smooth parametrization, we have developed a novel weighted spherical harmonic (SPHARM) representation, which generalizes the traditional SPHARM as a special case. For a specific choice of weights, the weighted-SPHARM is shown to be the least squares approximation to the solution of an isotropic heat diffusion on a unit sphere. The main aims of this paper are to present the weighted-SPHARM and to show how it can be used in the tensor-based morphometry. As an illustration, the methodology has been applied in the problem of detecting abnormal cortical regions in the group of high functioning autistic subjects.

**Index Terms**—Cortical surface, spherical harmonic (SPHARM), tensor-based morphometry.

## I. INTRODUCTION

**I**N many previous cortical morphometric studies, cortical thickness has been mainly used to quantify cortical shape variations in a population [13], [21], [27], [33]–[35]. The cortical thickness measures the amount of gray matter along the normal direction on a cortical surface. However, the gray matter growth can be characterized by both the normal and the tangential directions along the surface [13]. In this paper, we present a new tensor-based morphometry (TBM) that quantifies the amount of gray matter along the tangential direction via the concept of a *local area element*. The local area element is obtained from the Riemannian metric tensors, which are computed from the novel weighted spherical harmonic (SPHARM) representation [9]. We will review literature that are directly related to our methodology and address what our specific contributions are.

Unlike the deformation-based morphometry (DBM) [5], [12], [49], which uses deformation obtained from the nonlinear registration of brain images, TBM uses the high order spatial derivatives of deformation in constructing morphological tensor maps such as Jacobian determinant, torsion, and vorticity [4], [12], [13], [20], [44]. From these tensor maps, 3-D statistical para-

metric maps (SPM) are constructed to quantify variations in higher order changes of deformation fields. The main morphometric measure in the TBM is the Jacobian determinant of the deformation field since it directly measures tissue growth and atrophy. The advantage of TBM over DBM is that TBM can directly characterize tissue growth while DBM only characterizes the relative positional difference so the Jacobian determinant is a more relevant metric for quantifying tissue growth and atrophy [12]. In this study, the concept of the Jacobian determinant is generalized to a local area element via the Riemannian metric tensor formulation. Our local area element is the differential geometric generalization of the Jacobian determinant in Riemannian manifolds. So the area element can be used to quantify the tangential cortical tissue growth and atrophy directly.

As a subset of TBM, cortical surface specific morphometries have been developed [11], [13], [16], [45], [47]. Unlike 3-D whole brain volume based TBM, the surface specific morphometries have the advantage of providing a direct quantification of cortical morphology. Further, better sensitivity and specificity can be obtained in analyzing cortical surface specific morphometric changes [1], [13], [33]. The cerebral cortex is a 2-D highly convoluted sheet without any holes or handles topologically equivalent to a sphere [20]. Most of the features that distinguish these cortical regions can only be measured relative to the local orientation of the cortical surface [16]. It is likely that different clinical populations will exhibit different cortical surface geometry. By analyzing surface measures such as cortical thickness, curvatures, surface area, local area element, and fractal dimension, brain shape differences can be quantified locally along the cortical surface [13], [11], [45], [47]. Cortical surface analyses require the segmentation of tissue boundaries, which are mainly obtained as high-resolution triangle meshes from deformable surface algorithms [19], [16], [34]. The interface between gray and white matter is called the *inner surface* while the gray matter and cerebrospinal fluid (CSF) interface is called the *outer surface*. In this study, we will only use the outer surface for the local area element computation.

Once we have a triangular mesh as a realization of a cortical surface, surface related geometric quantities can be computed from the mesh. Due to the discrete nature of triangle mesh, surface parameterization is necessary for accurate and smooth estimation of the geometric quantities. Cortical surface parameterization has been mainly done by fitting a quadratic polynomial locally [13], [28], [29]. Then from this local parameterization, Gaussian and mean curvatures and the Riemannian metric tensors are computed to characterize cortical shape variations. However, the quadratic polynomial fit requires an accurate normal vector estimation, which tend to be highly unstable

Manuscript received July 18, 2007; revised January 15, 2008. First published February 8, 2008; last published July 25, 2008 (projected). *Asterisk indicates corresponding author.*

\*M. K. Chung is with the Department of Biostatistics and Medical Informatics, and the Waisman Laboratory for Brain Imaging and Behavior, University of Wisconsin, Madison, WI 53706 USA (e-mail: mkchung@wisc.edu).

K. M. Dalton and R. J. Davidson are with the Waisman Laboratory for Brain Imaging and Behavior, University of Wisconsin, Madison, WI 53706 USA.

Color versions of one or more of the figures in this paper are available online at <http://ieeexplore.ieee.org>.

Digital Object Identifier 10.1109/TMI.2008.918338

in triangle meshes [36], [53]. In contrast to this local approach, a global parameterization via SPHARM is also available [23], [24], [31], [40], [41]. This traditional SPHARM representation has been mainly used as a data reduction technique rather than obtaining high order spatial derivative information. Two-dimensional anatomical boundaries such as ventricle surfaces [23] and hippocampal surfaces [41] are parameterized by SPHARM and its coefficients are fed into statistical analyses such as a principal component analysis, a linear discriminant analysis, and support vector machines. The main geometric features are encoded in low degree spherical harmonic, while the noise will be in high degree spherical harmonics [24]. In this study, we generalize the traditional SPHARM by weighting its coefficients with exponentially decaying factors, and develop an iterative analytic differentiation framework for computing the Riemannian metric tensors. It will be shown that the weighted-SPHARM is a more generalized framework than the traditional SPHARM. Since we are not performing a finite difference based numerical differentiation, the tensor estimation should be more stable. Compared to the local polynomial fitting, our approach completely avoids estimating unstable normal vectors. The weighted-SPHARM tends to be computationally expensive compared to the local quadratic polynomial fitting while providing more accuracy and flexibility for a hierarchical representation.

In previous TBM, computations on a discrete triangle mesh produced significant mesh noise in cortical measure. In order to increase the signal-to-noise ratio (SNR) and the sensitivity of statistical analysis for cortical measure, cortical surface based data smoothing such *diffusion smoothing* was necessary [1], [8], [13], [33], [46]. The drawback of the diffusion smoothing is the complexity of setting up a finite element method (FEM) and making the numerical scheme stable [8], [13]. Since the weighted-SPHARM is mathematically equivalent to the diffusion smoothing [9] while it uses the exact analytical basis, it offers a more accurate numerical approximation over the diffusion smoothing without additional computation. Further, because the full-width at half-maximum (FWHM) of the smoothing kernel can be exactly computed in the weighted-SPHARM while it is only an asymptotic approximation in the diffusion smoothing [11], the random-field-theory-based statistical analysis can be used. This provides a more coherent and unified cortical surface analysis framework.

Once we compute the local area elements from the weighted-SPHARM, it is necessary to compare them across subjects via surface registration. Most previous surface registration methods are formulated as an optimization problem by minimizing an objective function that measures the global fit of two surfaces while maximizing the smoothness of the deformation in such a way that the gyral patterns are matched smoothly [11], [16], [18], [21], [38], [47]. These type of surface registration techniques are computationally expensive. In the weighted-SPHARM representation, the surface registration is straightforward and does not require any sort of optimizations explicitly. Corresponding surface positions are established by matching spherical harmonics [9]. This technique has an advantage of bypassing the computationally expensive optimization problem since the correspondence across subjects are built into the weighted-SPHARM representation itself.

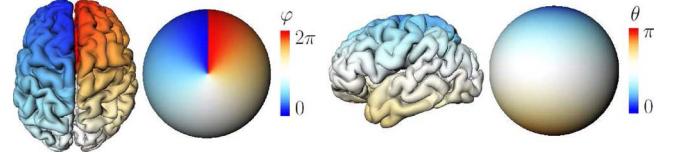


Fig. 1. Using the deformable surface algorithm that establish a mapping from a unit sphere to a cortical surface, we parameterize the cortical surface with the polar angle  $\theta$  and the azimuthal angle  $\varphi$ .

## II. PRELIMINARY

In this section, we introduce mathematical notations and basic concepts of SPHARM. Since there are variations on defining the associated Legendre polynomials and the spherical harmonics, it is necessary to clearly state the exact mathematical forms to minimize confusion. Many SPHARM literature [7], [23], [24], [41] use the complex-valued spherical harmonics while we are using the real-valued spherical harmonics since it is more intuitive to set up a statistical model.

### A. Surface Parametrization

Let  $\mathcal{M}$  and  $S^2$  be a cortical surface and a unit sphere, respectively.  $\mathcal{M}$  and  $S^2$  are realized as polygonal meshes with more than 80 000 triangle elements. It is natural to assume the cortical surface to be a smooth 2-D Riemannian manifold parameterized by two parameters [19]. This parametrization is constructed in the following way. A point  $u = (u_1, u_2, u_3) \in S^2$  is mapped to  $p = (x, y, z) \in \mathcal{M}$  via the mapping  $U$ , which is obtained by a deformable surface algorithm that preserves anatomical homology and the topological connectivity of meshes (Fig. 1). We will refer this mapping as the *spherical mapping*. Then we parameterize  $u$  by the spherical coordinates:

$$(u_1, u_2, u_3) = (\sin \theta \cos \varphi, \sin \theta \sin \varphi, \cos \theta)$$

with  $(\theta, \varphi) \in \mathcal{N} = [0, \pi] \otimes [0, 2\pi)$ . The polar angle  $\theta$  is the angle from the north pole and the azimuthal angle  $\varphi$  is the angle along the horizontal cross section of a MRI (Fig. 1).

The mapping from the parameter space  $\mathcal{N}$  to the unit sphere  $S^2$  will be denoted as  $X$ , i.e.,  $X : \mathcal{N} \rightarrow S^2$ . Then we have a composite mapping  $Z$  from the parameter space to the cortical surface:  $Z = U \circ X : \mathcal{N} \rightarrow \mathcal{M}$ .  $Z$  is a 3-D vector of surface coordinates and it will be stochastically modeled as

$$Z(\theta, \varphi) = \nu(\theta, \varphi) + \epsilon(\theta, \varphi) \quad (1)$$

where  $\nu$  is a unknown true differentiable parametrization and  $\epsilon$  is a random vector field on the unit sphere. The computation of the Riemannian metric tensors and the local area element require estimating differentiable function  $\nu$ .

### B. Spherical Harmonic Representation

The basis functions on a unit sphere are given as the eigenfunctions satisfying  $\Delta f + \lambda f = 0$ , where  $\Delta$  is the spherical Laplacian

$$\Delta = \frac{1}{\sin \theta} \frac{\partial}{\partial \theta} \left( \sin \theta \frac{\partial}{\partial \theta} \right) + \frac{1}{\sin^2 \theta} \frac{\partial^2}{\partial \varphi^2}.$$

There are  $2l + 1$  eigenfunctions, denoted as  $Y_{lm} (|m| \leq l)$ , corresponding to the same eigenvalue  $\lambda = l(l + 1)$ .  $Y_{lm}$  is

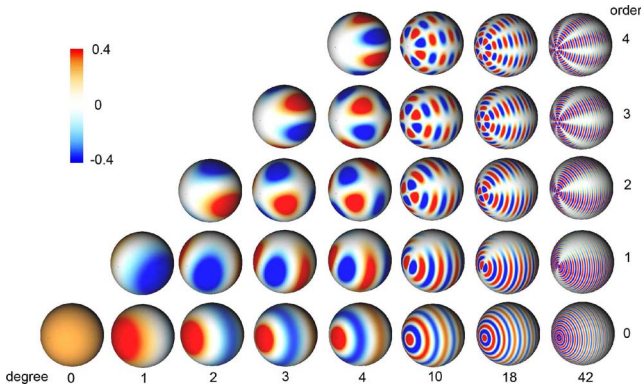


Fig. 2. Spherical harmonic basis of selective degree and orders. The center of the concentric circles at order  $m = 0$  is the north pole.

called the *spherical harmonic* of degree  $l$  and order  $m$  [15]. The explicit form of the  $2l + 1$  spherical harmonics of degree  $l$  is given by

$$Y_{lm} = \begin{cases} c_{lm} P_l^{|m|}(\cos \theta) \sin(|m|\varphi), & -l \leq m \leq -1 \\ \frac{c_{lm}}{\sqrt{2}} P_l^{|m|}(\cos \theta), & m = 0 \\ c_{lm} P_l^{|m|}(\cos \theta) \cos(|m|\varphi), & 1 \leq m \leq l \end{cases}$$

where  $c_{lm} = \sqrt{((2l+1)/2\pi)((l-|m|)!/(l+|m|)!)}$  and  $P_l^m$  is the *associated Legendre polynomial* of order  $m$ . Spherical harmonics of particular degrees and orders are illustrated in Fig. 2. For fixed  $l$ ,  $P_l^m$  form orthogonal polynomials over  $[-1, 1]$ . Following the convention used in Arfken [3], we have omitted the phase  $(-1)^m$  in the definition of the associated Legendre polynomial. Many previous SPHARM literature [7], [23], [24], [41] used the complex-valued spherical harmonics so the care is needed in comparing different numerical implementations of the associated Legendre polynomials and the spherical harmonics. The spherical harmonics form orthonormal bases on  $S^2$  such that

$$\int_{S^2} Y_{ij}(p) Y_{lm}(p) d\mu(p) = \begin{cases} 1, & \text{if } i = l, j = m \\ 0, & \text{otherwise.} \end{cases} \quad (2)$$

For  $f, h \in L^2(S^2)$ , the space of square integrable functions in  $S^2$ , the inner product is defined as

$$\langle f, h \rangle = \int_0^{2\pi} \int_0^\pi f(\theta, \varphi) h(\theta, \varphi) \sin \theta d\theta d\varphi$$

where the Lebesgue measure  $d\mu(\theta, \varphi) = \sin \theta d\theta d\varphi$ . Consider the subspace

$$\mathcal{H}_k = \left\{ \sum_{l=0}^k \sum_{m=-l}^l \beta_i Y_{lm} : \beta_i \in \mathbb{R} \right\} \subset L^2(S^2)$$

which is spanned by up to the  $k$ th degree spherical harmonics. We are interested in estimating  $f \in L^2(S^2)$  using a function in  $\mathcal{H}_k$ . The least squares estimation (LSE) of  $f$  in the subspace  $\mathcal{H}_k$  is then given by the finite Fourier series expansion.

*Theorem 1:*

$$\sum_{l=0}^k \sum_{m=-l}^l f_{lm} Y_{lm} = \arg \min_{h \in \mathcal{H}_k} \|f - h\|^2$$

where the norm is defined as  $\|f\| = \langle f, f \rangle^{1/2}$ .

This is the basis of the traditional SPHARM representation of closed anatomical boundaries [23], [24], [41].

### III. WEIGHTED-SPHARM

#### A. Basic Theory

The traditional SPHARM is only one possible representation of functional data measured on a unit sphere. We present a more general representation called the *weighted-SPHARM*, which weights the coefficients of the traditional SPHARM by the eigenvalues of a kernel. It can be shown that the traditional SPHARM is the special case of the weighted-SPHARM.

We start with the spectral representation of a positive definite kernel in  $S^2$ . Consider the positive definite kernel  $K(p, q)$  of the form

$$K(p, q) = \sum_{l=0}^{\infty} \sum_{m=-l}^l \lambda_{lm} Y_{lm}(p) Y_{lm}(q) \quad (3)$$

where the ordered eigenvalues

$$\lambda_{00} \geq \lambda_{1m_1} \geq \lambda_{2m_2} \geq \dots \geq 0$$

satisfy

$$\int_{S^2} K(p, q) Y_{lm}(q) d\mu(q) = \lambda_{lm} Y_{lm}(p). \quad (4)$$

This is the special case of the Mercer's theorem [15]. From (4), it follows that  $K$  is a reproducing kernel in  $L^2(S^2)$ . Without the loss of generality, we assume the kernel is normalized as

$$\int_{S^2} K(p, q) d\mu(q) = 1. \quad (5)$$

The smooth functional estimation  $h$  of measurement  $f$  is searched in  $\mathcal{H}_k$  that minimizes the integral of the weighted square distance between  $f$  and  $h$ .

*Theorem 2:*

$$\begin{aligned} \sum_{l=0}^k \sum_{m=-l}^l \lambda_{lm} f_{lm} Y_{lm} \\ = \arg \min_{h \in \mathcal{H}_k} \int_{S^2} \int_{S^2} K(p, q) |f(q) - h(p)|^2 d\mu(p) d\mu(q). \end{aligned}$$

We will call the finite expansion given in Theorem 2 as the weighted-SPHARM representation. The theorem can be proved by substituting  $h = \sum_{l=0}^k \sum_{m=-l}^l c_{lm} Y_{lm}(p)$  and optimizing with respect to  $c_{lm}$ .

Define kernel smoothing as the integral convolution

$$K * f(p) = \int_{S^2} f(q) K(p, q) d\mu(q). \quad (6)$$

$$= \sum_{l=0}^{\infty} \sum_{m=-l}^l \lambda_{lm} \langle f, Y_{lm} \rangle Y_{lm}(p). \quad (7)$$

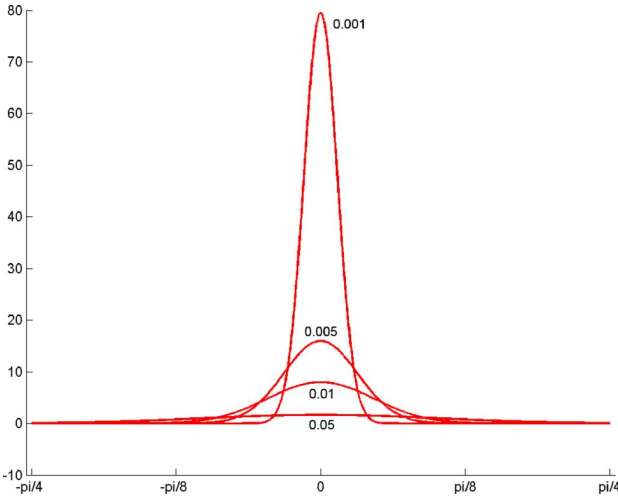


Fig. 3. The shape of the heat kernel  $K_\sigma(p, q)$  for various bandwidths  $\sigma$ . The shape is computed from the harmonic addition theorem and (16). The point  $p$  is fixed to be the north pole and the horizontal axis is the angle  $\cos^{-1}(p \cdot q)$ .

The last equation is obtained by substituting (3) into (6). The (7) shows that the weighted-SPHARM is the finite expansion of kernel smoothing. Kernel smoothing (3) can be further shown to be the minimizer of the following integral.

*Theorem 3:* For a fixed point  $p \in S^2$

$$K * f(p) = \arg \min_{h \in L^2(S^2)} \int_{S^2} K(p, q) [f(q) - h]^2 d\mu(q). \quad (8)$$

This theorem can be proved by differentiating the integral with respect to  $h$ .

For the choice of eigenvalues  $\lambda_{lm} = e^{-l(l+1)\sigma}$  the corresponding kernel is called the *heat kernel* or Gauss-Weistrass kernel [7], [11], [39] and it will be denoted as

$$K_\sigma(p, q) = \sum_{l=0}^{\infty} \sum_{m=-l}^l e^{-l(l+1)\sigma} Y_{lm}(p) Y_{lm}(q). \quad (9)$$

The parameter  $\sigma$  determines the spread of kernel as shown in Fig. 3. As  $\sigma \rightarrow 0$ ,  $\lambda_{lm} \rightarrow 1$  and the heat kernel  $K_\sigma(p, q) \rightarrow \delta(p-q)$ , the Dirac-delta function. So the traditional SPHARM is a special case of the weighted-SPHARM. It is interesting to note that even though the regularizing cost functions are different in Theorem 1 and 2, they are related asymptotically.

Another interesting property of the weighted-SPHARM is observed by noting that  $K_\sigma * f$  is the unique solution of the isotropic heat diffusion

$$\frac{\partial g}{\partial t} = \Delta g, \quad g(p, t=0) = f(p) \quad (10)$$

at time  $t = \sigma^2/2$  [9], [11], [39]. Hence, the weighted-SPHARM is the finite expansion of the isotropic heat diffusion. Instead of solving the heat equation numerically, which tends to be unstable [1], [13], the weighted-SPHARM representation provides a more stable approach. In a similar approach, Bulow used spherical harmonics in developing isotropic heat diffusion via the Fourier transform on a unit sphere as form of hierarchical surface representation [7].

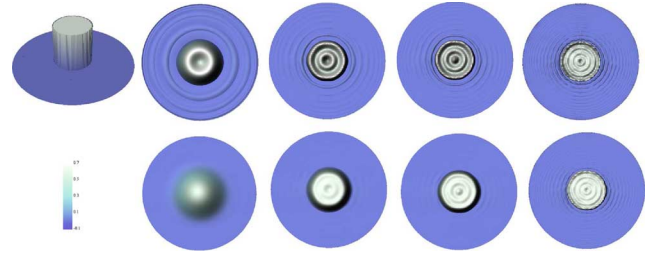


Fig. 4. The first column is a hat shaped 3-D step function. The weighted-SPHARM (bottom) of the step function at different bandwidths ( $\sigma = 0.01, 0.001, 0.0005, 0.0001$ ) and the corresponding traditional SPHARM (top) of the same degree. The weighted-SPHARM has less ringing artifacts.

There are two main advantages of using the weighted-SPHARM over the traditional SPHARM. The weighted-SPHARM reduces the substantial amount of the Gibbs phenomenon (ringing artifacts) [9], [22] that is associated with the convergence of a Fourier series. Either discontinuous or rapidly changing measurements will have slowly decaying Fourier coefficients and thus the traditional SPHARM representation converges slowly. However, the weighted-SPHARM additionally weights the Fourier coefficients with the exponentially decaying weights contributing to more rapid convergence. The Gibbs phenomenon is visually demonstrated in Fig. 4 with a hat-shaped step function ( $z = 1$  if  $x^2 + y^2 < 1$  and  $z = 0$  if  $1 \leq x^2 + y^2 \leq 2$ ). The bottom figures are the weighted-SPHARM at different scales ( $\sigma = 0.01, 0.001, 0.0005, 0.0001$ ), and the top figures are the corresponding traditional SPHARM of the same degree. The degree selection process is discussed in the next section. The top figures exhibit significant ringing artifacts while the bottom figures show less ringing artifacts.

The second advantage of using the weighted-SPHARM is related to heat kernel smoothing formulation used in the random field theory [11], [51], [52]. The random field theory that is needed to correct for multiple comparisons requires the smoothness of signal, as measured as the FWHM of the heat kernel. In the traditional SPHARM, the heat kernel degenerates to the Dirac-delta function so we cannot apply the random field theory directly.

## B. Numerical Implementation

The eigenvalues  $\lambda_{lm}$  are given analytically from a given kernel. So we only need to numerically compute the Fourier coefficients  $f_{lm}$  in the weighted-SPHARM representation. Previously, the computation for the Fourier coefficients computation for the Fourier coefficients was based on the direct numerical integration over high-resolution triangle meshes with more than 80 000 triangles and the average intervertex distance of 0.0189 mm [10]. Unfortunately, the direct numerical integration is extremely slow and it is not practical when high degree spherical harmonics are needed. So we have recently developed a new numerical technique called the *iterative residual fitting* (IRF) algorithm [9], [40]. Compared to the numerical integration, which takes more than few hours, the IRF algorithm takes only about 5 min per subject for computing all the coefficients up to degree 78 in a personal computer.

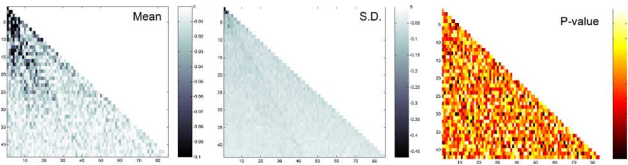


Fig. 5. The mean (left) and the standard deviation (middle) of the Fourier coefficients for 28 subjects. The vertical axis is the degree and the horizontal axis is the order arranged from the lowest to the highest. Right: The  $p$ -value of a Jarque–Bera test for normality. Smaller  $p$ -values indicate the tendency for nonnormality. Only 10 out of total 1849 coefficients show nonnormality at  $\alpha = 0.05$  level.

The IRF algorithm estimates the Fourier coefficients iteratively by breaking a large least squares problem in the subspace  $\mathcal{H}_k$  into smaller subspaces. Let us decompose the subspace  $\mathcal{H}_k$  into the smaller subspaces as the direct sum  $\mathcal{H}_k = \mathcal{I}_0 \oplus \mathcal{I}_1 \cdots \oplus \mathcal{I}_k$ , where the subspace

$$\mathcal{I}_l = \left\{ \sum_{m=-l}^l \beta_{lm} Y_{lm}(p) : \beta_{lm} \in \mathbb{R} \right\}$$

is spanned by the  $l$ th degree spherical harmonics only. Then the IRF algorithm estimates the Fourier coefficients  $f_{lm}$  in each subspace  $\mathcal{I}_l$  iteratively from degree 0 to  $k$ . This hierarchical estimation from lower to higher degree is possible due to the orthonormality of spherical harmonics. The technical detail of the IRF algorithm, numerical implementation, accuracy issues are given in [9] and [40]. The MATLAB implementation of IRF is freely available online<sup>1</sup> with a sample outer cortical surface.

While increasing the degree of the weighted-SPHARM increases the goodness-of-fit, it also increases the number of coefficients to be estimated quadratically. So it is necessary to find the optimal degree where the goodness-of-fit and the number of parameters balance out. In most previous SPHARM literature [23], [24], [40], [41], the degree is simply selected based on a prespecified error bound that depends on the size of an anatomical structure. We have adapted a model selection framework [37] that does not depend on the size of the anatomical structure.

The Fourier coefficients  $f_{lm}$  can be modeled to follow independent normal distribution  $N(\mu_{lm}, \sigma_l^2)$ . Within the same degree, equal variance is assumed. We have checked the model assumption on our data set. Fig. 5 shows the sample mean and variance of the Fourier coefficients for the  $x$ -coordinates of 28 subjects. The vertical direction is the degree  $k$  and the horizontal direction is the order arranged from  $-k$  to  $k$ . The third figure shows the  $p$ -value of testing normality using a Jarque–Bera statistic [26]. Only 10 out of total  $(42 + 1)^2 = 1849$  coefficients show nonnormality at  $\alpha = 0.05$  level indicating our normality assumption is valid. We have also computed cross correlation of all  $1849^2$  pairs of coefficients to check independence (Fig. 6). Note that Gaussian random variables are independent if cross correlations are zero. The most pairs show extremely low correlation and the average correlation is 0.16 indicating the independence assumption is valid.

<sup>1</sup>http://www.stat.wisc.edu/~mchung/software/weighted-SPHARM.html

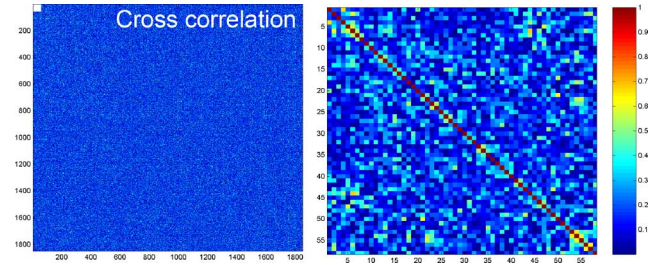


Fig. 6. Left: cross correlation of up to 42° SPHARM coefficients. Right: enlargement of a small white square in the left figure. Cross correlation map shows very low correlation in most pairs. Average correlation is 0.16.

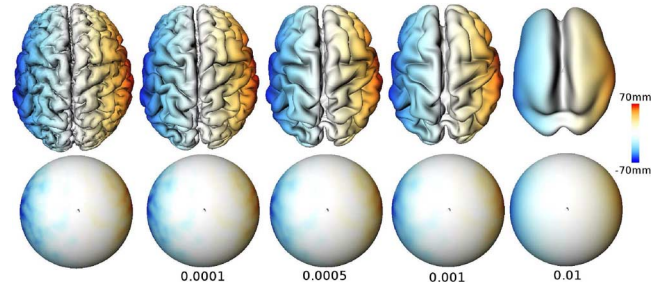


Fig. 7. The weighted-SPHARM representation at different bandwidths. The first column is the original cortical surface. The color bar indicates  $x$ -coordinate values. The second row shows the result mapped on a unit sphere. The black dot in the center indicates the north pole.

The above model assumption is equivalent to the following linear model:

$$f(p_i) = \sum_{l=0}^k \sum_{m=-l}^l e^{-\lambda(\lambda+1)\sigma} \mu_{lm} Y_{lm}(p_i) + \epsilon(p_i) \quad (11)$$

where  $\epsilon$  is a zero mean isotropic Gaussian random field. Once we determined all the coefficients up to the  $k$ th degree using the IRF algorithm, we check if adding the next terms  $\mu_{k+1,-(k+1)}, \dots, \mu_{k+1,k+1}$  to the  $k$ th degree model (11) is statistically significant in a forward model section framework [9], [37]. If the corresponding  $p$ -value of the test statistic [37], [50] is bigger than the prespecified significance level of 0.05, we stop the iteration. If not, we increase the degree and repeat the process. For bandwidths  $\sigma = 0.01, 0.001, 0.0005, 0.0001$ , the optimal degrees are 18, 42, 52, 78, respectively (Fig. 7).

We have compared the IRF result against the analytical solution of (10). For any arbitrary initial condition of the form

$$f = \sum_{l=0}^k \sum_{m=-l}^l \alpha_{lm} e^{l(l+1)} Y_{lm} \in \mathcal{H}_k \quad (12)$$

the solution to (10) is given by

$$K_\sigma * f = \sum_{l=0}^k \sum_{m=-l}^l \alpha_{lm} Y_{lm}. \quad (13)$$

Comparing the analytical solution (13) to the result obtained from the IRF algorithm serves as the basis for validation. It is sufficient to use a single term in (12) for validation. Let  $f = e^{l(l+1)} Y_{lm}$  be an initial condition of (10). Then the solution of

TABLE I  
FWHM AND ACCURACY FOR THE WFS REPRESENTATION

degree $l$	order $m$	bandwidth $\sigma$	FWHM	mean error	$f_{lm}$
18	17	0.01	0.3456	0.0575	0.9995
42	41	0.001	0.1257	0.0126	0.9992
52	51	0.0005	0.0968	0.0101	0.9988
78	77	0.0001	0.0597	0.0068	0.9984

(10) is given by  $K_\sigma * f = Y_{lm}$ . Table I shows the comparison for various degrees and orders. The fifth column shows the mean absolute error between the theoretical value  $Y_{lm}$  and the numerical result obtained from the IRF algorithm. The mean is taken over all mesh vertices. The last column shows the numerical computation of integral  $\int_{S^2} Y_{lm}^2(p) d\mu(p) = 1$ . Table I shows our numerical implementation provides sufficiently good numerical accuracy.

#### IV. TENSOR-BASED MORPHOMETRY

Taking weighted-SPHARM as a global parameterization for cortical surface  $\mathcal{M}$ , we can compute the Riemannian metric tensors that are needed in computing the local area element.

##### A. Metric Tensor Estimation

The weighted-SPHARM estimation  $\hat{\nu}$  of the unknown true parametrization  $\mu$  in (1) is given by

$$\hat{\nu}(\theta, \varphi) = \sum_{l=0}^k \sum_{m=-l}^l \lambda_{lm} Z_{lm} Y_{lm}$$

with  $Z_{lm} = \langle Z, Y_{lm} \rangle$ . For this study, we used Eigenvalue  $\lambda_{lm} = e^{-l(l+1)\sigma}$  corresponding to the heat kernel. The Riemannian metric tensors  $g_{ij}$  will be computed by analytically differentiating the weighted-SPHARM. The estimation of the Riemannian metric tensors requires partial derivatives of  $\hat{\nu}$ . Denoting the partial differential operators as  $\partial_1 = \partial_\theta$  and  $\partial_2 = \partial_\varphi$ , we have

$$\partial_i \hat{\nu} = \sum_{l=0}^k \sum_{m=-l}^l \lambda_{lm} Z_{lm} \partial_i Y_{lm}(\theta, \varphi).$$

The derivatives of spherical harmonics can be analytically computed. We start with the derivative for the associated Legendre polynomials

$$\partial_\theta P_l^{|m|}(x) = l \cot \theta P_l^{|m|}(x) - (l + |m|) \sin^{-1} \theta P_{l-1}^{|m|}(x)$$

where  $x = \cos \theta$ . Note that  $P_{l-1}^{|m|} = 0$  if  $|m| \geq l$ . The recursive formula introduces a numerical singularity at the north and south poles ( $\theta = 0, \pi$ ) so we have chosen the poles to be the regions of noninterest that connect the left and the right hemispheres (Fig. 1). Then the derivatives of spherical harmonics are expressed as the functions of spherical harmonics

$$\partial_\theta Y_{lm} = l \cot \theta Y_{lm} - (l + |m|) \frac{c_{lm}}{c_{l-1,m}} \sin^{-1} \theta Y_{l-1,m}$$

with the convention  $Y_{l-1,m} = 0$  if  $|m| \geq l$ . The constant in the second term can be further simplified as

$$(l + |m|) \frac{c_{lm}}{c_{l-1,m}} = \sqrt{\frac{2l+1}{2l-1}} (l^2 - m^2).$$

The derivative with respect to  $\varphi$  is simply given as

$$\partial_\varphi Y_{lm} = -m Y_{l,-m}.$$

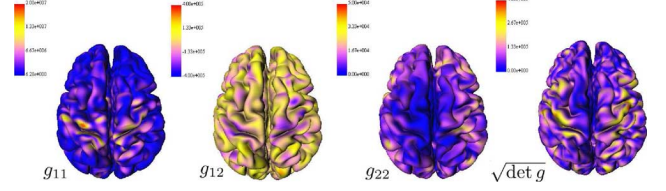


Fig. 8. Metric tensor estimation. The metric tensors  $g_{ij}$  are estimated by analytically differentiating the weighted-SPHARM representation. The local area element  $\sqrt{\det g}$  measures the amount of area expansion and shrinking with respect to the parameter space  $\mathcal{N}$ .

This recursive relation reduces the computational time by recycling the spherical harmonics used in estimating the SPHARM coefficients.

The  $3 \times 2$  Jacobian matrix  $J$  of mapping from parameter space  $\mathcal{N}$  to cortical surface  $\mathcal{M}$  is given by  $J = (\partial_\theta \hat{\nu}, \partial_\varphi \hat{\nu})$ . The Riemannian metric tensors are  $g = (g_{ij}) = J^t J$ . The component is given by  $g_{ij} = \partial_i \hat{\nu} \cdot \partial_j \hat{\nu}$  with the vector inner product  $\cdot$ . The Riemannian metric tensors measure the amount of deviation of a cortical surface from a flat Euclidean plane. If the cortical surface is flat, we obtain  $g_{ij} = \delta_{ij}$ , the identity matrix. The Riemannian metric tensors enable us to compute the local *area element*  $\sqrt{\det g}$ . The area element measures the amount of the transformed area in  $\mathcal{M}$  of the unit area in the parameterized space  $\mathcal{N}$  via the mapping  $\nu$ . Fig. 8 shows the estimation of the metric tensors for a subject. Using the area element, the total surface area of  $\mathcal{M}$  can be written as

$$\mu(\mathcal{M}) = \int_0^{2\pi} \int_0^\pi \sqrt{\det g}(\theta, \varphi) d\theta d\varphi.$$

Locally, surface deformation can be decomposed into the tangential and the normal components with respect to a surface normal vector [13]. At each point  $p$ , we define *local gray matter volume* as  $V(p) = \sqrt{\det g(p)} C(p)$ , where  $C$  is cortical thickness. Then the total gray matter volume is approximately given as  $\int_{S^2} V(p) d\mu(p)$ . The gray matter volume will change if either the area element increases (tangential expansion) or cortical thickness increases (normal expansion). Then the change in the gray matter volume is the sum of the change in local area and the change in cortical thickness [13]

$$\frac{dV}{V} = \frac{d\sqrt{\det g}}{\sqrt{\det g}} + \frac{dC}{C}.$$

The change in the local area element can be viewed as to contributing to the tangential component of the gray matter volume change.

The scale invariant area element is defined as  $\sqrt{\det g}/\mu(\mathcal{M})$ , where the total surface area  $\mu(\mathcal{M})$  is estimated by summing the area of triangles in a mesh. Fig. 9 shows the scale invariant area element for randomly selected 12 subjects. Although the scale invariant area element is invariant under affine scaling, it is not invariant under different parameterizations such as conformal mappings [2], [24], [25], quasi-isometric mappings [48] and area preserving mappings [6], [41], [43]. Considering these parameterizations introduce area distortion, it is necessary to use a parameterization invariant metric for a stable statistical analysis. This can be obtained by directly measuring the area expansion.

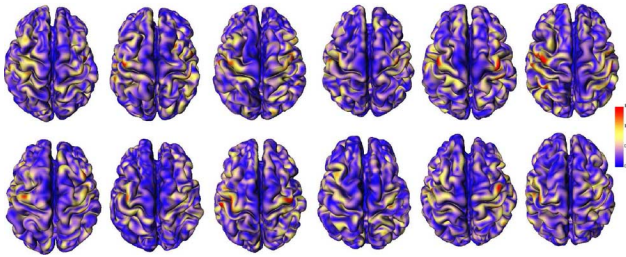


Fig. 9. Scale invariant area elements for randomly selected six control subjects (top) and six autistic subjects (bottom). The color scale is thresholded at 1.5 (150%) for better visualization. With respect to the parameter space  $\mathcal{N}$ , there is up to 300% area expansion.

sion rate with respect to a template surface  $\mathcal{M}_0$  rather than the parameter space  $\mathcal{N}$ . Consider a mapping from the template  $\mathcal{M}_0$  to the cortical surface  $\mathcal{M}$ . The Jacobian of this mapping will be noted as  $J_0$ . The Jacobian  $J_0$  is expected to be invariant under different parameterizations and only depends on the registration between the two surfaces. Let  $g_0$  be the metric tensors of  $\mathcal{M}_0$ . The area element of  $\mathcal{M}$  is  $\sqrt{\det g} = \det J_0 \sqrt{\det g_0}$ . Then the parameterization invariant measure is obtained by simply computing the percentage change of area expansion with respect to the template as

$$\frac{\sqrt{\det g} - \sqrt{\det g_0}}{\sqrt{\det g_0}} = \det J_0 - 1 \quad (14)$$

giving a local area related measure invariant under parameterization. This quantity is called the *surface area dilatation* and it is approximately the trace of the Jacobian determinant [12]. Our methodology does not work for area-preserving mappings since the Jacobian determinant is 1. For this singular case, we compute the Jacobian determinant directly from the surface registration result.

### B. Statistical Inference on Unit Sphere

For the  $i$ th subject ( $1 \leq i \leq m$ ), we denote the cortical surface as  $\mathcal{M}_i$  and its parameterization invariant surface Jacobian determinant  $\det J_i(\theta, \varphi)$ . Then we have the following general linear model (GLM):

$$\det J_i(\theta, \varphi) = \beta_0 + \beta_1(\theta, \varphi) \cdot \text{group}_i + \epsilon(\theta, \varphi)$$

where  $\epsilon$  is a mean zero Gaussian random field and  $\text{group}_i$  is a categorical dummy variable (0 for autism and 1 for control). We are interested in localizing any group differences in the local area element map by testing if  $\beta_1(\theta, \varphi) = 0$  for all  $(\theta, \varphi)$ . At each fixed point  $(\theta, \varphi)$ , the test statistic  $T(\theta, \varphi)$  is a two sample  $t$ -statistic with  $m - 2$  degrees-of-freedom. Since we need to perform the test at every points  $(\theta, \varphi)$ , this becomes a multiple comparison problem. We used the random field theory [50]–[52] based thresholding to determine the statistical significance. The  $p$ -value for the one sided alternate hypothesis, i.e.,  $\beta_1 > 0$ , is given by

$$p(\theta, \varphi) = P \left[ \sup_{p \in S^2} T(p) > t(\theta, \varphi) \right] \approx \sum_{d=0}^2 R_d(S^2) \rho_d(h) \quad (15)$$

where  $R_d$  is the  $d$ -dimensional *resels* of  $S^2$  and  $\rho_d$  is the  $d$ -dimensional *Euler characteristic (EC) density* of a  $T$ -field with  $m - 2$  degrees of freedom, and  $t(\theta, \varphi)$  is the observed two sample  $t$ -statistic at  $(\theta, \varphi)$ . The resels are

$$R_0(S^2) = 2, R_1(S^2) = 0, R_2(S^2) = \frac{\mu(S^2)}{\text{FWHM}^2}$$

where FWHM is the full-width at half-maximum of the weighted-SPHARM. The mathematical formulas for the EC-densities are given in [51]. Although there are some variations in defining resels and EC-density through the literature [50]–[52], we have used the convention used in [52]. Fig. 10 shows the resulting corrected  $p$ -value map showing highly localized regions of abnormal pattern in autistic subjects. The  $p$ -value map is projected on the average cortical surface of 38 subjects used in the study. We have used the threshold  $h = \pm 5.19$  corresponding to the corrected  $p$ -value of 0.05.

In computing the corrected  $p$ -value, it is necessary to compute the FWHM but it is not trivial since there is no known close form expression for the FWHM as a function of  $\sigma$ . So the FWHM is computed numerically. The heat kernel can be simplified from (9), via the harmonic addition theorem [3], as

$$K_\sigma(p, q) = \sum_{l=0}^{\infty} \frac{2l+1}{4\pi} e^{-l(l+1)\sigma} P_l^0(\cos \vartheta) \quad (16)$$

where  $\vartheta$  is the angle between  $p$  and  $q$ , i.e.,  $\cos \vartheta = p \cdot q$ . By fixing  $p$  to be the north pole, i.e.,  $\varphi = 0$  and  $p = (0, 0, 1)$  while varying  $q = (\sin \vartheta, 0, \cos \vartheta)$  for  $0 \leq \vartheta = \cos^{-1}(p \cdot q) \leq \pi$ , we can obtain the shape of heat kernel and its corresponding FWHM numerically for each  $\sigma$  (Fig. 3). Table I shows the FWHM for various bandwidths  $\sigma$ . In previous diffusion and heat kernel smoothing [13], [11], between 20–30 mm FWHM was used. The FWHM used in this study is extremely small since the analysis is performed on a unit sphere rather than a larger cortical surface. However, the comparable resels can be obtained by using the bandwidth of  $\sigma = 0.001$  corresponding to the FWHM of 0.1257 mm.

## V. APPLICATION TO AUTISM STUDY

Three Tesla  $T_1$ -weighted MR scans were acquired for 16 high functioning autistic and 12 control right-handed males. Sixteen autistic subjects were diagnosed via The Autism Diagnostic Interview–Revised (ADI-R) used by a trained and certified psychologist at the Waisman center at the University of Wisconsin-Madison [17]. The average ages are  $17.1 \pm 2.8$  and  $16.1 \pm 4.5$  for control and autistic group, respectively. Image intensity nonuniformity was corrected using a nonparametric nonuniform intensity normalization method [42] and then the image was spatially normalized into the Montreal Neurological Institute (MNI), Montreal, QC, Canada, stereotaxic space using a global affine transformation [14]. Afterwards, an automatic tissue-segmentation algorithm based on a supervised artificial neural network classifier was used to classify each voxel into three classes: CSF, gray matter, and white matter [32].

Triangular meshes for outer cortical surfaces were obtained by the anatomic segmentation using the proximities (ASP)

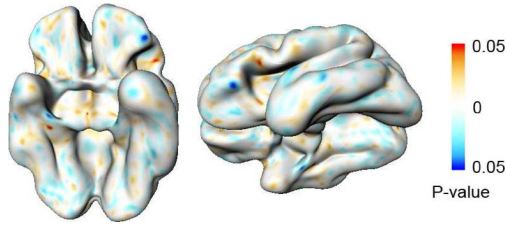


Fig. 10. The  $p$ -value map projected on the average weighted-SPHARM surface of 28 subjects. The  $p$ -value is thresholded at 0.05 using the random field theory. The focalized red (blue) regions show more (less) surface area in the autistic subjects compared to the controls.

method [34], which is a variant of deformable surface algorithms. The algorithm generates 40 962 vertices and 81 920 triangles with the identical mesh topology for all subjects. The vertices indexed identically on two cortical meshes will have a very close anatomic homology [13], [30], [34]. The mesh starts as a sphere located outside the brain and is shrunk to match the cortical boundary by minimizing a cost function that contains the image, stretch, bending, and vertex-to-vertex proximity terms. The deformation in the MNI stereotaxic coordinate system combined with stretch constraints that limit the movement of vertices, effectively enforces a relatively consistent placement of points on the cortical surface. This provides the same spherical parameterization at identically indexed vertices across different cortical surfaces.

If we detect anatomical changes along the inner surface, it is unclear if the changes are due to changes in gray or white matters, or possibly both. On the other hand, changes in the outer cortical surface are the direct consequence of changes in the gray matter. Choosing the outer surface representation reduces the ambiguity of interpreting the statistical result. Therefore, we have chosen the outer surface over the inner surface for the study.

Once we obtained the outer cortical surfaces of 28 subjects, the weighted-SPHARM representation were constructed. We have used the bandwidth  $\sigma = 0.001$  corresponding to degree  $k = 42$ . The corresponding FWHM is 0.1257 mm. The Fourier coefficients were estimated using the IRF algorithm. The corresponding surface positions across two different weighted-SPHARM surfaces are obtained by matching the harmonics of the same degree and order via the *SPHARM-correspondence* [9]. This is equivalent to obtaining the optimal displacement, in the least squares sense, by taking the difference between the two weighted-SPHARM representations.

Using the weighted-SPHARM representation, area elements and corresponding surface Jacobian determinants are analytically computed, and compared across subjects. The two sample  $t$ -statistic map is computed and its corrected  $p$ -value map is projected on the average weighted-SPHARM surface of 28 subjects (Fig. 10). The average surface is constructed by averaging the Fourier coefficients within the spherical harmonic of the same degree and order. The average surface serves as an anatomical landmark for showing where group differences are located.

We performed the random field theory based multiple comparison correction on the computed  $t$ -statistic map. Fig. 10 shows the regions of statistically significant group difference

thresholded at  $\alpha = 0.05$  level (corresponding to the  $t$ -value of  $\pm 5.19$ ). Although there are other regions of group difference, the left inferior frontal gyrus show the most significant group difference.

## VI. CONCLUSION

In this paper, we presented the weighted-SPHARM representation and its application in TBM. The weighted-SPHARM is used as a differentiable parametrization of the cortex. Based on a new iterative formulation, spatial derivatives of the weighted-SPHARM are computed and used to derive metric tensors and an area element. The ratio of area elements is then used to compute the surface Jacobian determinant invariant under parameterization. The surface Jacobian determinant is used in determining statistically significant regions of abnormal cortical tissue expansion and shrinking for autistic subjects.

The weighted-SPHARM is a very flexible function estimation technique for scalar and vector data defined on a unit sphere. We have shown that the weighted-SPHARM is related to heat kernel smoothing. Since heat kernel smoothing is related to isotropic heat diffusion [9], [13], [39], we were able to connect our new representation to the isotropic heat diffusion. This argument can be further extended. By choosing a kernel induced from a particular self-adjoint partial differential equation (PDE), we can construct the least squares estimation of the PDE without numerically solving it [9]. This should serve as a spring board for investigating other PDE-based data smoothing techniques in the weighted-SPHARM framework.

## ACKNOWLEDGMENT

The authors would like to thank P. Thompson of the Laboratory of Neuro Imaging at UCLA for the discussion on the area element and the surface Jacobian determinant. The authors would also like to thank R. Hartley of the Department of Systems Engineering at the Australian National University for the discussion on the weighted-SPHARM representation and positive definite kernels on spheres.

## REFERENCES

- [1] A. Andrade, F. Kherif, J. Mangin, K. J. Worsley, A. Paradis, O. Simon, S. Dehaene, D. Le Bihan, and J.-B. Poline, "Detection of fMRI activation using cortical surface mapping," *Hum. Brain Mapp.*, vol. 12, pp. 79–93, 2001.
- [2] S. Angenent, S. Hacker, A. Tannenbaum, and R. Kikinis, "On the laplace-beltrami operator and brain surface flattening," *IEEE Trans. Med. Imag.*, vol. 18, no. 8, pp. 700–711, Aug. 1999.
- [3] G. B. Arfken, *Mathematical Methods for Physicists*, 5th ed. New York: Academic, 2000.
- [4] J. Ashburner, C. Good, and K. J. Friston, "Tensor based morphometry," *NeuroImage*, vol. 11S, p. 465, 2000.
- [5] J. Ashburner, C. Hutton, R. S. J. Frackowiak, I. Johnsrude, C. Price, and K. J. Friston, "Identifying global anatomical differences: Deformation-based morphometry," *Hum. Brain Mapp.*, vol. 6, pp. 348–357, 1998.
- [6] C. Brechbuhler, G. Gerig, and O. Kubler, "Parametrization of closed surfaces for 3-D shape description," *Comput. Vis. Image Understand.*, vol. 61, pp. 154–170, 1995.
- [7] T. Bulow, "Spherical diffusion for 3-D surface smoothing," *IEEE Trans. Pattern Anal. Mach. Intell.*, vol. 26, no. 12, pp. 1650–1654, Dec. 2004.
- [8] A. Cachia, J.-F. Mangin, D. Rivière, D. Papadopoulos-Orfanos, F. Kherif, I. Bloch, and J. Régis, "A generic framework for parcellation of the cortical surface into gyri using geodesic voronoi diagrams," *Image Anal.*, vol. 7, pp. 403–416, 2003.

- [9] M. K. Chung, L. Shen, K. M. Dalton, A. C. Evans, and R. J. Davidson, "Weighted Fourier representation and its application to quantifying the amount of gray matter," *IEEE Trans. Med. Imag.*, vol. 26, pp. 566–581, Apr. 2007.
- [10] M. K. Chung, "Heat kernel smoothing on unit sphere," in *Proc. IEEE Int. Symp. Biomed. Imag. (ISBI)*, Apr. 2006, pp. 992–995.
- [11] M. K. Chung, S. Robbins, R. J. Davidson, A. L. Alexander, K. M. Dalton, and A. C. Evans, "Cortical thickness analysis in autism with heat kernel smoothing," *NeuroImage*, vol. 25, pp. 1256–1265, 2005.
- [12] M. K. Chung, K. J. Worsley, T. Paus, D. L. Cherif, C. Collins, J. Giedd, J. L. Rapoport, and A. C. Evans, "A unified statistical approach to deformation-based morphometry," *NeuroImage*, vol. 14, pp. 595–606, 2001.
- [13] M. K. Chung, K. J. Worsley, S. Robbins, T. Paus, J. Taylor, J. N. Giedd, J. L. Rapoport, and A. C. Evans, "Deformation-based surface morphometry applied to gray matter deformation," *NeuroImage*, vol. 18, pp. 198–213, 2003.
- [14] D. L. Collins, P. Neelin, T. M. Peters, and A. C. Evans, "Automatic 3-D intersubject registration of MR volumetric data in standardized talairach space," *J. Comput. Assist. Tomogr.*, vol. 18, pp. 192–205, 1994.
- [15] R. Courant and D. Hilbert, *Methods of Mathematical Physics*. New York: Interscience, 1953.
- [16] A. M. Dale and B. Fischl, "Cortical surface-based analysis I. Segmentation and surface reconstruction," *NeuroImage*, vol. 9, pp. 179–194, 1999.
- [17] K. M. Dalton, B. M. Nacewicz, T. Johnstone, H. S. Schaefer, M. A. Gernsbacher, H. H. Goldsmith, A. L. Alexander, and R. J. Davidson, "Gaze fixation and the neural circuitry of face processing in autism," *Nature Neurosci.*, vol. 8, pp. 519–526, 2005.
- [18] C. Davatzikos, "Spatial transformation and registration of brain images using elastically deformable models," *Comput. Vis. Image Understand.*, vol. 66, pp. 207–222, 1997.
- [19] C. Davatzikos and R. N. Bryan, "Using a deformable surface model to obtain a shape representation of the cortex," in *Proc. IEEE Int. Conf. Comput. Vis.*, 1995, vol. 9, pp. 2122–2127.
- [20] C. Davatzikos, M. Vaillant, S. M. Resnick, J. L. Prince, S. Letovsky, and N. Bryan, "A computerized approach for morphological analysis of the corpus callosum," *J. Comput. Assist. Tomogr.*, vol. 20, pp. 88–97, 1996.
- [21] B. Fischl, M. I. Sereno, R. Tootell, and A. M. Dale, "High-resolution intersubject averaging and a coordinate system for the cortical surface," *Hum. Brain Mapp.*, vol. 8, pp. 272–284, 1999.
- [22] A. Gelb, "The resolution of the Gibbs phenomenon for spherical harmonics," *Math. Computat.*, vol. 66, pp. 699–717, 1997.
- [23] G. Gerig, M. Styner, D. Jones, D. Weinberger, and J. Lieberman, "Shape analysis of brain ventricles using SPHARM," in *IEEE Workshop Math Methods Biomed. Image Anal.*, 2001, pp. 171–178.
- [24] X. Gu, Y. L. Wang, T. F. Chan, T. M. Thompson, and S. T. Yau, "Genus zero surface conformal mapping and its application to brain surface mapping," *IEEE Trans. Med. Imag.*, vol. 23, no. 8, pp. 949–958, Aug. 2004.
- [25] M. K. Hurdal and K. Stephenson, "Cortical cartography using the discrete conformal approach of circle packings," *NeuroImage*, vol. 23, p. S119S128, 2004.
- [26] C. M. Jarque and A. K. Bera, "A test for normality of observations and regression residuals," *Int. Stat. Rev.*, vol. 55, pp. 1–10, 1987.
- [27] S. E. Jones, B. R. Buchbinder, and I. Aharon, "Three-dimensional mapping of cortical thickness using Laplace's equation," *Human Brain Mapp.*, vol. 11, pp. 12–32, 2000.
- [28] S. C. Joshi, U. Grenander, and M. I. Miller, "The geometry and shape of brain sub-manifolds," *Int. J. Pattern Recognit. Artif. Intell.*, vol. 11, pp. 1317–1343, 1997.
- [29] S. C. Joshi, J. Wang, M. I. Miller, D. C. Van Essen, and U. Grenander, "On the differential geometry of the cortical surface," *Vis. Geometry IV*, pp. 304–311, 1995.
- [30] N. Kabani, D. Le Goualher, G. MacDonald, and A. C. Evans, "Measurement of cortical thickness using an automated 3-D algorithm: A validation study," *NeuroImage*, vol. 13, pp. 375–380, 2000.
- [31] A. Kelemen, G. Szekely, and G. Gerig, "Elastic model-based segmentation of 3-D neuroradiological data sets," *IEEE Trans. Med. Imag.*, vol. 18, no. 10, pp. 828–839, Oct. 1999.
- [32] K. Kollakian, "Performance analysis of automatic techniques for tissue classification in magnetic resonance images of the human brain," M.S. thesis, Concordia Univ., Montreal, QC, Canada, 1996.
- [33] J. P. Lerch and A. C. Evans, "Cortical thickness analysis examined through power analysis and a population simulation," *NeuroImage*, vol. 24, pp. 163–173, 2005.
- [34] J. D. MacDonald, N. Kabani, D. Avis, and A. C. Evans, "Automated 3-D extraction of inner and outer surfaces of cerebral cortex from MRI," *NeuroImage*, vol. 12, pp. 340–356, 2000.
- [35] M. I. Miller, A. B. Massie, J. T. Ratnanather, K. N. Botteron, and J. G. Csernansky, "Bayesian construction of geometrically based cortical thickness metrics," *NeuroImage*, vol. 12, pp. 676–687, 2000.
- [36] D. L. Page, A. Koschan, Y. Sun, J. Paik, and M. A. Abidi, "Robust crease detection and curvature estimation of piecewise smooth surfaces from triangle mesh approximations using normal voting," *Comput. Vis. Pattern Recognit. (CVPR)*, vol. I, pp. 162–167, 2001.
- [37] C. R. Rao and H. Toutenburg, *Linear Models: Least Squares and Alternatives*. New York: Springer, 1999.
- [38] S. M. Robbins, "Anatomical standardization of the human brain in Euclidean 3-Space and on the cortical 2-manifold," Ph.D. dissertation, School Comput. Sci., McGill Univ., Montreal, QC, Canada, 2003.
- [39] S. Rosenberg, *The Laplacian on a Riemannian Manifold*. Cambridge, U.K.: Cambridge Univ. Press, 1997.
- [40] L. Shen and M. K. Chung, "Large-scale modeling of parametric surfaces using spherical harmonics," in *Proc. 3rd Int. Symp. 3-D Data Process., Visualization Transmission (3DPVT)*, Chapel Hill, NC, 2006, pp. 294–301.
- [41] L. Shen, J. Ford, F. Makedon, and A. Saykin, "Surface-based approach for classification of 3-D neuroanatomical structures," *Intell. Data Anal.*, vol. 8, pp. 519–542, 2004.
- [42] J. G. Sled, A. P. Zijdenbos, and A. C. Evans, "A nonparametric method for automatic correction of intensity nonuniformity in MRI data," *IEEE Trans. Med. Imag.*, vol. 17, no. 1, pp. 87–97, Feb. 1998.
- [43] M. Styner, I. Oguz, S. Xu, C. Brechbuhler, D. Pantazis, J. Levitt, M. Shenton, and G. Gerig, "Framework for the statistical shape analysis of brain structures using SPHARM-pdm," in *Insight J.*, 2006, pp. 1–22.
- [44] P. M. Thompson, J. N. Giedd, R. P. Woods, D. MacDonald, A. C. Evans, and A. W. Toga, "Growth patterns in the developing human brain detected using continuum-mechanical tensor mapping," *Nature*, vol. 404, pp. 190–193, 2000.
- [45] P. M. Thompson, K. M. Hayashi, G. de Zubicaray, A. L. Janke, S. E. Rose, J. Semple, D. Herman, M. S. Hong, S. S. Dittmer, D. M. Dordrell, and A. W. Toga, "Dynamics of gray matter loss in Alzheimer's disease," *J. Neurosci.*, vol. 23, pp. 994–1005, 2003.
- [46] P. M. Thompson, K. M. Hayashi, G. de Zubicaray, A. L. Janke, S. E. Rose, J. Semple, M. S. Hong, D. H. Herman, D. Gravano, D. M. Dordrell, and A. W. Toga, "Mapping hippocampal and ventricular change in Alzheimer disease," *NeuroImage*, vol. 22, pp. 1754–1766, 2004.
- [47] P. M. Thompson and A. W. Toga, "A surface-based technique for warping 3-dimensional images of the brain," *IEEE Trans. Med. Imag.*, vol. 15, no. 4, pp. 402–417, 1996.
- [48] B. Timsari and R. Leahy, "An optimization method for creating semi-isometric flat maps of the cerebral cortex," in *Proc. SPIE Med. Imag.*, 2000, pp. 698–708.
- [49] L. Wang, J. S. Swank, I. E. Glick, M. H. Gado, M. I. Miller, J. C. Morris, and J. G. Csernansky, "Changes in hippocampal volume and shape across time distinguish dementia of the Alzheimer type from healthy aging," *NeuroImage*, vol. 20, pp. 667–682, 2003.
- [50] K. J. Worsley, "Detecting activation in fMRI data," *Stat. Methods Med. Res.*, vol. 12, pp. 401–418, 2003.
- [51] K. J. Worsley, S. Marrett, P. Neelin, A. C. Vandal, K. J. Friston, and A. C. Evans, "A unified statistical approach for determining significant signals in images of cerebral activation," *Human Brain Mapp.*, vol. 4, pp. 58–73, 1996.
- [52] K. J. Worsley, J. E. Taylor, F. Tomaiuolo, and J. Lerch, "Unified univariate and multivariate random field theory," *NeuroImage*, vol. 23, pp. S189–195, 2004.
- [53] P. Yuen, N. Khalili, and F. Mokhtarian, "Curvature estimation on smoothed 3-D meshes," in *Proc. Br. Mach. Vis. Conf.*, 1999, pp. 133–142.